



Water vapor saturation and ice cloud occurrence in the atmosphere of Mars

Loïc Poncin^{a,b}, Armin Kleinböhl^{a,*}, David M. Kass^a, R. Todd Clancy^c, Shohei Aoki^{d,1},
Ann Carine Vandaele^d

^a Jet Propulsion Laboratory, California Institute of Technology, Pasadena, CA, USA

^b École Supérieure des Techniques Aéronautiques et de Construction Automobile, Paris, France

^c Space Science Institute, Boulder, CO, USA

^d Royal Belgian Institute for Space Aeronomy, Brussels, Belgium

ARTICLE INFO

Keywords:

Mars atmosphere
Water vapor
Water ice clouds
Saturation
MCS

ABSTRACT

We investigate water vapor saturation in the martian atmosphere in the presence or proximity of water ice clouds. We evaluate mixing ratio profiles of ambient water vapor derived from measurements by the Compact Reconnaissance Imaging Spectrometer for Mars (CRISM) and the Nadir and Occultation for Mars Discovery (NOMAD) instrument in comparison with saturated vapor mixing ratio profiles derived from co-located temperature measurements by the Mars Climate Sounder (MCS). We find that during the aphelion season the average saturation state of the atmosphere is close to saturation in the presence of clouds, with supersaturation ratios reaching values of no more than two to three towards the top of the cloud layer. During the perihelion season, subseasonally averaged water vapor is close to saturation or somewhat subsaturated in the presence of clouds, with some supersaturation at southern high latitudes towards the top of the clouds. Measurements at northern mid- to high latitudes during a Global Dust Storm suggest a shift of the cloud occurrence to higher altitudes but exhibit a similar saturation structure, with supersaturations not exceeding a ratio of five. The atmosphere above cloud layers is largely subsaturated, suggesting that cloud formation is fairly instantaneous upon the temperature dropping below the frost point and high levels of supersaturation are not required to form water ice clouds. We propose a schematic model of cloud evolution in which small cloud particles are formed rapidly in slightly supersaturated regions, and then fall and grow such that ice opacity is still observed even in the subsaturated regions below.

1. Introduction

The vertical distribution of water vapor and its relation to ice cloud occurrence in the martian atmosphere has been a longstanding question. Saturation and cloud formation are major factors that constrain the vertical distribution of water vapor. The altitude at which water vapor saturation occurs is largely controlled by the thermal structure of the atmosphere. The saturation altitude of water varies on a seasonal scale, with low atmospheric temperatures at low latitudes in northern spring and summer leading to the formation of the aphelion cloud belt (ACB), creating a hygro-pause and largely restricting the propagation of water vapor to altitudes above 40 km (Clancy et al., 1996). The increased dust activity in southern spring and summer leads to higher temperatures and shifts the hygro-pause upwards, leading to the formation of water ice clouds at 40–60 km altitude (McCleese et al., 2010). Global dust events

can lead to water vapor being transported to altitudes in excess of 70 km (Aoki et al., 2019), allowing the formation of ice clouds at these altitudes (Heavens et al., 2018; Kleinböhl et al., 2020). On a diurnal scale, water vapor saturation is influenced by the diurnal tide as evidenced by the strong correlation between tidally driven temperature structure and ice cloud occurrence, where peaks in water ice opacity are typically found below local temperature minima (Lee et al., 2009).

The vertical distribution of water vapor has recently gained additional interest with the recognition that middle atmospheric water vapor can photolyze, leading to the formation of hydrogen, which in turn can propagate to the upper atmosphere and escape, leading to increased water loss from Mars (Chaffin et al., 2017). Hence the transport of water vapor to the middle atmosphere influences the hydrogen escape rate (Chaffin et al., 2021) and quantifying its variation with season and in response to dust storm occurrence might help explain this contribution to

* Corresponding author. Jet Propulsion Laboratory, Mail-Stop 169-237, 4800, Oak Grove Dr., Pasadena, CA, USA.
E-mail address: armin.kleinboehl@jpl.nasa.gov (A. Kleinböhl).

¹ Now at: Institute of Space and Astronautical Science, Japan Aerospace Exploration Agency, Sagami-hara, Japan

hydrogen escape. Water ice cloud occurrence observed in the middle atmosphere has been used as a proxy for middle atmospheric water vapor (Heavens et al., 2018) so knowledge of the saturation state of the atmosphere is important to constrain the accuracy of this proxy.

The saturation state of water vapor in the martian middle atmosphere allows us to better understand the mechanisms behind the planet's water cycle and how efficient the ascent of water vapor to the upper atmosphere is. It is widely assumed that water vapor in the presence of water ice clouds usually is in saturation or near saturation, and that supersaturation is a rare behavior in the cold martian atmosphere. Detailed microphysical model simulations (Daerden et al., 2010) applied to explain the boundary layer clouds detected by the Phoenix LIDAR (Whiteway et al., 2009) found that a supersaturation ratio of only 10% was sufficient to explain the LIDAR observations. These clouds formed in conditions similar to those in the terrestrial stratosphere, and the supersaturation ratios were similar to those found on Earth. However, results from the Spectroscopy for the Investigation of the Characteristics of the Atmosphere of Mars (SPICAM) instrument onboard Mars Express have suggested that water vapor profiles often indicate some level of supersaturation in the aphelion season, with supersaturation ratios reaching 2 to 10 (Maltagliati et al., 2011). No widespread supersaturation was found in the perihelion season (Maltagliati et al., 2013). These observations of supersaturation have been attributed to the removal of dust particles from the atmosphere, also known as scavenging (Maltagliati et al., 2011). Much like droplets of water during rain on Earth, ice particles clean regions of the middle atmosphere by colliding and capturing dust particles while falling through the atmosphere and depositing them in lower layers of the atmosphere. Therefore, in absence of condensation nuclei in the middle atmosphere, water vapor is unable to condense below the frost point temperature of water, which leads to a state of supersaturation in some regions of the atmosphere. More recently, this view has been challenged as findings from the Atmospheric Chemistry Suite (ACS) onboard the ExoMars Trace Gas Orbiter (TGO) suggest supersaturation even in the presence of dust and ice clouds (Fedorova et al., 2020). ACS observed widespread supersaturation over a large vertical range, with saturation ratios frequently exceeding a value of 10 and even reaching values over 100. This suggests that even though condensation nuclei are present in the middle atmosphere, the process of condensation would have to be overpowered by a process that would allow for water vapor to become supersaturated in cloudy conditions, such as rapid drops in temperature and/or rises in water concentration (Fedorova et al., 2020).

In this paper, we study water vapor saturation in the presence or proximity of clouds in the martian atmosphere by intercomparisons of water vapor profiles, derived from measurements by the Compact Reconnaissance Imaging Spectrometer for Mars (CRISM) onboard the Mars Reconnaissance Orbiter (MRO) and by the Nadir and Occultation for Mars Discovery (NOMAD) instrument onboard TGO, with saturated water profiles, derived from temperature measurements by the Mars Climate Sounder (MCS) onboard MRO. We provide a description of the instruments and the relevant datasets in section 2. We describe the methodology used for analysis in section 3 and present our results in section 4. We provide a discussion of our results and outline our understanding of the saturation state of the atmosphere in conditions of cloud occurrence and the evolution of water ice particles in section 5. We finally summarize our conclusions in section 6.

2. Measurements

2.1. MCS onboard MRO

2.1.1. Instrument

The Mars Climate Sounder (MCS, McCleese et al., 2007) is one of six instruments onboard of the Mars Reconnaissance Orbiter (MRO, Zurek and Smrekar, 2007). MCS is a passive 9-channel infrared thermal emission radiometer which views the martian atmosphere in limb, nadir and

off-nadir geometries. It consists of two telescopes of identical design that are mounted on a double gimbal which allows it to have degrees of freedom in both azimuth and elevation. The MCS spectral bands include five mid-infrared channels, three far-infrared channels, and one visible/near-infrared channel. Each channel consists of a linear array of 21 uncooled thermopile detectors, which instantaneously measures a radiance profile when vertically pointed at the limb. This allows MCS to observe characteristics of the atmosphere from the surface to about 80 km altitude with a vertical resolution close to 5 km when pointing at the Mars limb. Each single measurement has an integration time of about 2 s. Typically five consecutive limb measurements are averaged and combined with one or two co-located nadir or off-nadir measurements to provide a combined radiance dataset for profile retrieval of atmospheric parameters.

2.1.2. Dataset

From the radiance profiles measured by MCS, vertical profiles of temperature, dust extinction and H₂O ice extinction are retrieved over a vertical range from near the surface to about 80 km altitude with a ~5 km vertical resolution (Kleinböhl et al., 2009, 2011). Temperature retrievals use absorption in three channels covering the strong CO₂ band around 660 cm⁻¹. Retrievals of dust extinction are based on a dust absorption feature centered at 463 cm⁻¹. Dust retrievals during a Global Dust Storm (GDS) of MY34 additionally use a far infrared channel centered at 316 cm⁻¹ in order to extend the retrievable vertical range (Kleinböhl et al., 2020). Retrievals of H₂O ice extinction are based on a water ice absorption feature centered at 843 cm⁻¹. In conditions of high ice opacity as found in the ACB the retrieval of ice is supported by a far infrared channel at 254 cm⁻¹ (Kleinböhl et al., 2017a). Retrieved quantities are reported on a regular pressure grid. In addition, an altitude scale referenced to the surface is reported based on spacecraft pointing information. Profiles retrieved from measurements along the orbit track of the MRO spacecraft are corrected for lateral gradients using a two-dimensional radiative transfer scheme (Kleinböhl et al., 2017b). Retrieved temperature profiles have a precision of 0.5–2 K in most atmospheric conditions, based on signal-to-noise ratio and the quality of the radiance fit. Inter-comparison studies suggest that agreement with contemporaneous and historical temperature measurements is typically within 2–3 K (Kleinböhl et al., 2009; Hinson et al., 2014; Shirley et al., 2015). Dust and water ice extinction profiles have typical precisions of 10⁻⁴ – 10⁻⁵ km⁻¹ (Kleinböhl et al., 2009). In this work we use an extinction of 10⁻⁴ km⁻¹ at 843 cm⁻¹ as a threshold for the robust detection of a water ice cloud. The data relevant to this study was obtained over seven years on a campaign basis between July 2009 and December 2016, and during MY34 dusty season between April 2018 and March 2019 (see Tables 1 and 2). MCS radiances and retrieved geophysical quantities are stored as ASCII files and made available for public use through NASA's Planetary Data System (PDS).

2.2. CRISM onboard MRO

2.2.1. Instrument

The Compact Reconnaissance Imaging Spectrometer for Mars (CRISM) is also one of the six instruments onboard of MRO. CRISM is a 544-channel visible and infrared imaging spectrometer which nominally views the martian atmosphere in nadir geometry (Murchie et al., 2007). CRISM covers a spectral range of 362–3920 nm with a spectral sampling of 6.55 nm. It consists of a Ritchey-Cretien telescope working along with two spectrometers, one in the visible/near-infrared and one in the infrared wavelength range, mounted on a one-axis gimbal to allow for targeted in-track measurements. The instrument has a multispectral untargeted mapping mode, a hyperspectral targeted mapping mode and an atmospheric mapping mode. This makes it possible to observe minerals on the surface with a horizontal resolution close to 15–19 m per pixel over a swath 10.8 km wide when in targeted mode and either 100 or 200 m per pixel over most of the planet using a subset of 72 wavelengths

Table 1

Summary of MCS observations in coordination with CRISM used in this work. Each entry is one campaign of CRISM limb observations. Longitude assignments correspond to the approximate longitudes of Hellas (H), Tharsis (T), Meridiani (M) and Valles Marineris (V).

Campaign	Date	Year	MY	L_s	Longitudes	Number of half-orbits
1	July 10, 11	2009	29	301°	H, T	2
2	February 10	2010	30	50°	T	1
3	April 7	2010	30	74°	H, T	2
4	April 28, 29	2010	30	83 – 84°	H, T	2
5	May 26	2010	30	96°	H, T	2
6	August 22, 23	2010	30	137°	0°, -100° – 150°	7
7	October 17	2010	30	166°	H, T	2
8	December 5, 6	2010	30	193°	H, T	2
9	March 31, April 1	2011	30	265°	H, T	2
10	May 14, 15	2011	30	292° – 293°	H, T	2
11	June 28,	2011	30	319°	H, T	2
12	August 22, 23	2011	30	349°	H, T	2
13	September 13	2011	31	0°	H, T	2
14	December 10, 11	2011	31	41° – 42°	H, T	2
15	April 24, 26	2012	31	101° – 102°	H, T, M	3
17	November 14, 15, 16	2012	31	206° – 208°	H, M, V	3
18	January 8, 9	2013	31	241°	M, V	2
19	March 7	2013	31	277°	H	1
21	December 11, 13	2013	32	61° – 62°	M, V	2
22	February 5, 6	2014	32	86°	H, V	2
26	February 13, 14	2015	32	290° – 291°	H, M	2
27	April 15, 17	2015	32	326° – 327°	H, M, V	3
28	August 31, September 1, 4	2015	33	35° – 37°	H, M, V	3
29	October 25, 30, 31	2015	33	59° – 62°	H, M, V	3
30	December 20, 23, 25	2015	33	84° – 86°	H, M, V	3
31	February 28, March 5, 6	2016	33	115° – 118°	H, M, V	3
32	May 10, 11, 15	2016	33	150° – 153°	H, M, V	3
33	July 3, 5, 6	2016	33	179° – 181°	H, M, V	3
34	August 30	2016	33	213°	H	1
36	December 21	2016	33	284°	M	1

when in multispectral mode. The atmospheric mode takes advantage of the other modes to perform emission-phase functions (EPF) around a targeted area by taking 10 additional spatially binned snapshots before and after the area. Indeed both scattering and absorption by aerosols and attenuation by atmospheric gases vary among snapshots of the same area and allow the instrument to study characteristics of the layers of the atmosphere above that area (Murchie et al., 2007, 2009).

Due to the limited range of its gimbal, CRISM does not nominally perform observations of the limb. However, changing the pitch orientation of the MRO spacecraft by 16.6° in the forward or aft direction enables CRISM to view the limb in that direction (Smith et al., 2013). This has been done on a campaign basis from July 2009 through April 2017, typically targeting orbit passes over Tharsis and Hellas in daytime. In April 2012 an orbit pass close to the prime meridian was added to the limb observation sequence (Clancy et al., 2017). During each CRISM limb observation the instrument repeatedly scans upwards and downwards across the limb in a mode that averages 10 pixels in each spatial direction, providing a spatial sampling of about 800 m at the tangent point. During each orbit pass CRISM limb scans are spaced roughly 10° in latitude (Smith et al., 2013). CRISM limb scans allow the observation of dust and water ice profiles (Smith et al., 2013), mesospheric clouds (Clancy et al., 2019), as well as O₂ airglow at 1.27 μm (Clancy et al., 2012, 2017) and OH airglow in the Meinel bands (Clancy et al., 2013).

2.2.2. Dataset

The CRISM dataset used for this study is based on limb observations of the 1.27 μm band emission of O₂(Δ_g) dayglow (Clancy et al., 2017). Volume emission rates (VER) in photons/cm³/second are retrieved based on radiative transfer modeling of limb measurements in the CRISM IR channel at altitudes below 60 km. Retrievals are obtained with a 3 km vertical resolution, which are interpolated to a standard 4 km altitude grid referenced to the areoid. Because O₂ and H₂O are anti-correlated in the martian atmosphere, the O₂ VERs can be used to derive water vapor content in the martian atmosphere. Clancy et al. (2017) use the LMDGCM

- a General Circulation Model with photochemistry of the martian atmosphere by the Laboratoire de Météorologie Dynamique (Lefèvre et al., 2004, 2008) - to establish a correlation between O₂ and H₂O at comparable locations (latitude, longitude), seasons (L_s), and local times to each 4 km gridded O₂(Δ_g) profile retrieval. Doing so allows for the comparison of CRISM ambient O₂(Δ_g) dayglow VER with LMDGCM modeled H₂O vapor number density (cm⁻³) as a function of modeled O₂(Δ_g).

The CRISM-derived water vapor profiles employed the LMDGCM simulated O₂(Δ_g) and water vapor profiles in point-by-point (location and time) comparisons, whereby the LMDGCM modeled water vapor abundance is scaled by the inverse ratio of CRISM observed to LMDGCM modeled O₂(Δ_g) volume emission. This analysis assumes that the LMDGCM photochemistry, including heterogeneous chemistry, accurately simulates Mars O₃ photochemistry. A recent comparison of SPICAM column measurements for Mars O₃ and H₂O (Lefèvre et al., 2021) suggests there is a negative 20–40% bias in LMDGCM O₃ simulated abundances employing heterogeneous chemistry, which is of the order of that estimated for the CRISM O₂(Δ_g) based H₂O derivation (30%). These SPICAM column comparisons are primarily reflective of O₃ and H₂O abundances in the lower ~ 10 km of the atmosphere, which is not sampled by the current analysis. However, if they were to apply it to altitudes above 10 km, then the CRISM-derived water vapor values employed in the current analysis could be biased ~ 30% too low, due to an as yet undefined error in our understanding of Mars O₃ photochemistry. The data relevant to this study were retrieved over seven years between campaign 1 in July 2009 and campaign 36 in December 2016 (see Table 1).

2.3. NOMAD onboard TGO

2.3.1. Instrument

The Nadir and Occultation for MArS Discovery (NOMAD) is one of four instruments onboard of the ExoMars Trace Gas Orbiter (TGO).

Table 2

Summary of key parameters of the co-located measurements between MCS and NOMAD used in this work.

Family	Date	Year	MY	L_s	Latitudes	Local times	Number of MCS/NOMAD measurements
1	August 31	2018	34	241.1° – 241.3°	52.0°N – 56.0°N	14.7 – 15.8	4/1
2	September 4	2018	34	243.7° – 243.8°	55.0°N – 60.8°N	14.4 – 15.3	7/1
3	September 5	2018	34	244.0° – 244.1°	55.6°N – 60.7°N	14.6 – 15.2	4/1
4	September 6	2018	34	244.6° – 244.7°	57.1°N – 60.5°N	14.6 – 15.1	3/1
5	February 10, 11, 12, 13	2019	34	338.9° – 340.6°	85.3°S – 76.0°S	22.7 – 1.6	19/7
6	February 16, 17, 19, 20, 21	2019	34	342.2° – 344.8°	78.4°S – 70.6°S	18.5 – 21.1	17/10
7	February 23, 24, 26	2019	34	345.6° – 347.3°	68.7°S – 62.1°S	18.1 – 20.0	7/4

NOMAD is a 3-channel spectrometer which views the martian atmosphere in limb, nadir and solar occultation (SO) geometries (Neefs et al., 2015; Patel et al., 2017; Vandaele et al., 2018). The instrument itself is pointed towards the center of Mars during nadir observations whereas limb and SO observations are done through solar-pointing periscopes inclined with respect to the nadir direction by 67.07°. This makes it possible to observe characteristics of the layers of the atmosphere from the surface to 200 km with a vertical resolution close to 2 km when pointing at the Mars limb with an integration time for a single measurement of about 1 s.

NOMAD scans the atmosphere using 3 spectrometers within 3 spectral intervals: Solar Occultation (SO, Neefs et al., 2015), Limb Nadir and Occultation (LNO, Neefs et al., 2015), and Ultraviolet and Visible Spectrometer (UVIS, Patel et al., 2017). The SO spectrometer observes in the infrared (covering 2.3 – 4.3 μm) and is capable of doing SO measurements through a periscope. The LNO spectrometer also observes in the infrared (covering 2.3 – 3.8 μm) and has an optical layout very similar to that of SO. However, it is capable of doing both nadir and limb on top of SO measurements by operating a flipping mirror mechanism. LNO has one periscope for limb and SO observations, and one cut-out hole in the NOMAD cover for nadir observations. The UVIS spectrometer has a dual-telescope system that receives and transmits observed light using a system of optical fibers. It observes in ultraviolet and visible wavelength ranges (covering 200 – 650 nm) and is capable of doing nadir and SO measurements. UVIS has one periscope for SO observations, and one cut-out hole in the NOMAD cover for nadir observations.

2.3.2. Dataset

NOMAD H₂O vapor density and volume mixing ratio (VMR) are retrieved using radiative transfer modeling of SO measurements by the SO channel. In SO geometry, NOMAD observes the Sun's light through the atmosphere from very high altitude down to the surface (Aoki et al., 2019). NOMAD uses a transmittance calculation algorithm developed for the reduction of SOIR (Solar Occultation in the Infrared) data, a SO channel from the Spectroscopy for Investigation of Characteristics of the Atmosphere of Venus (SPICAV) spectrometer onboard of Venus Express (Trompet et al., 2016; Aoki et al., 2019). Retrievals of H₂O vapor number density are done using the “onion peeling” method starting from the top of the atmosphere at 120 km of altitude with 1 km altitude step increments (Aoki et al., 2019; Vandaele et al., 2019). Measurements of diffraction order 134 (spectral range: 3011 – 3035 cm^{-1}) and 168 (spectral range: 3783 – 3803 cm^{-1}) are both analyzed independently and used to calculate H₂O vapor content in the martian atmosphere, reported on an altitude grid referenced to the areoid (Aoki et al., 2019).

The data relevant to this study was retrieved during the MY34 dusty season between April 21, 2018 and March 7, 2019 (see Table 2). The number density of water vapor along the line of sight is retrieved at each tangential altitude using the method to retrieve water vapor abundances from NOMAD as described in Aoki et al. (2019). The atmospheric temperatures and pressures assumed in the radiative transfer calculation are the ones predicted by GEM-Mars for MY 34 (Neary et al., 2020). For this work the retrieved water vapor number densities were used to recalculate volume mixing ratios using atmospheric densities from MCS (see Section 3.1.2).

3. Methods

3.1. Coordinated observations

3.1.1. Coordinated observations between CRISM and MCS

Part of this study was motivated by the publication of seasonal zonal averages of water vapor content from CRISM derived from O₂(Δ_g) dayglow emission rates. Table 1 in Clancy et al. (2017) details all CRISM observations taken into account for the calculation of six zonal and subseasonal averages of water vapor between $L_s = 30^\circ$ and $L_s = 360^\circ$. Water vapor content derived from O₂(Δ_g) dayglow retrievals covers the whole martian year thanks to data retrieved from 36 CRISM limb observation campaigns over seven years between July 2009 and December 2016.

Operating from the same spacecraft as CRISM, MCS was able to perform limb/on-planet measurements in coordination with most CRISM limb measurements. In total we were able to cross-reference 70 daylight half-orbits of MCS measurements taken nearly simultaneously with CRISM.

Table 1 summarizes all MCS and CRISM daylight half-orbits that were taken into account in this intercomparison study. For nearly all coordinated campaigns MCS was viewing along the MRO orbit track but toward the opposite limb from CRISM, introducing a time difference of about 15 min between MCS and CRISM limb measurements over the same area. MCS was viewing the forward limb (in the direction of travel of the MRO spacecraft) while CRISM was viewing the aft limb (opposite to the direction of travel of the MRO spacecraft) for campaigns 3 to 16, and CRISM was viewing the forward limb while MCS was viewing the aft limb for campaigns 1 and 17 to 36. Only for campaign 2 both CRISM and MCS were pointed at the forward limb. CRISM limb measurements for campaigns 16 and 35 were not used by Clancy et al. (2017) to compute zonal averages, so for the sake of consistency we did not use MCS data retrieved during these specific campaigns, either. Fig. 1 shows examples of transects of temperature, dust extinction, and water ice extinction as measured by MCS during two CRISM limb campaigns in the clear as well as the dusty season. Note that particularly in conditions of the ACB, cloud opacities in limb geometry can be too high in the infrared for MCS to obtain useable retrievals, limiting the useable altitude range in such conditions.

CRISM data are provided as zonal averages between 6 and 54 km altitude above the areoid and between -90° and 90° in latitude (each cell is 10° wide and 4 km tall). Each individual MCS temperature, dust extinction and water ice extinction profile is first used to estimate water vapor VMR at saturation above the areoid (see Methods). Then, individual profiles are sorted into daylight half-orbits, and finally MCS data are binned to match CRISM zonal grid, requiring a minimum of three measurements per bin. During CRISM campaigns 23 to 25, MCS was either stowed or viewing at an azimuth nearly perpendicular to the orbit track, preventing coordinated measurements with CRISM. We computed new zonal averages of CRISM water vapor for two periods of L_s ($L_s \in [100^\circ, 140^\circ]$ and $L_s \in [140^\circ, 200^\circ]$) by excluding these three measurement campaigns. Analogously to Clancy et al. (2017) we require to have at least two measurements in each latitude/altitude bin for these averages.

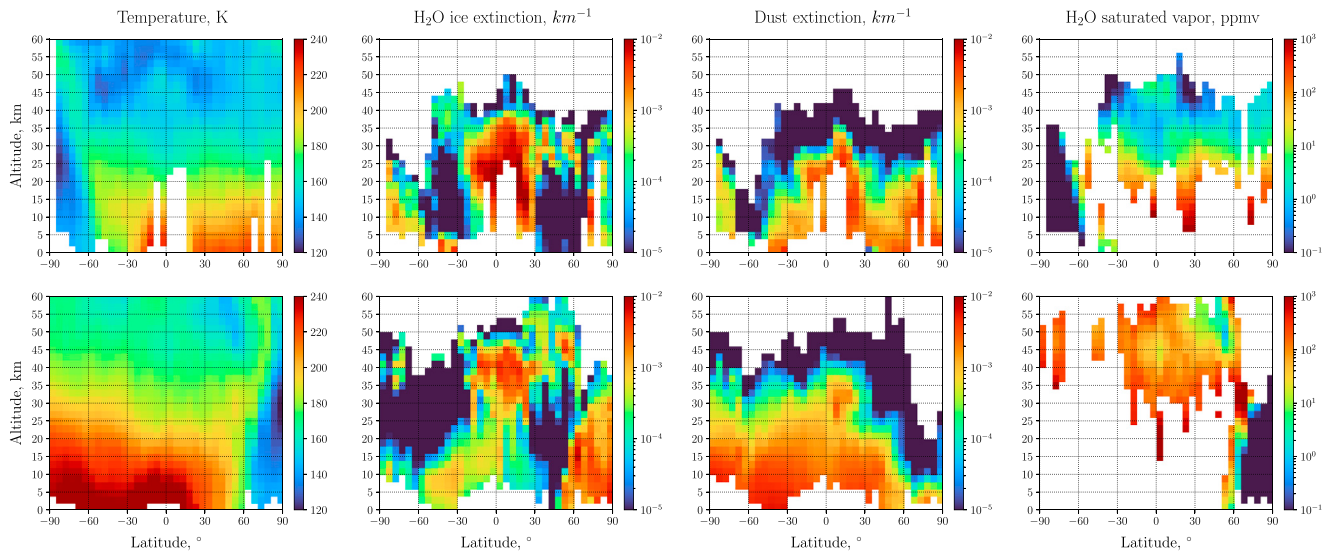


Fig. 1. Transects of measured temperature, water ice extinction, dust extinction and derived saturated water vapor by MCS in coordination with CRISM limb observations. Shown are an example each during the clear season (top, retrieved on April 29th, 2010 at $L_s = 83.82^\circ$ above the Hellas Planitia longitude corridor) and during the dusty season (bottom, retrieved on May 15th, 2011 at $L_s = 292.88^\circ$ above the Hellas Planitia longitude corridor).

3.1.2. Coordinated observations between NOMAD and MCS

In addition to comparisons with water vapor derived from CRISM we evaluate comparisons with water vapor as measured by the NOMAD instrument in solar occultation geometry from ExoMars TGO (Aoki et al., 2019). Part of these intercomparisons are based on serendipitous co-located observations between MCS and NOMAD during the global dust event in 2018. In addition, MCS can use its azimuth actuator to perform coordinated measurements with NOMAD by actively slewing to view towards the NOMAD observation point (López-Valverde et al., 2018). MCS performed coordinated observations with NOMAD from February 15 to March 7, 2019, in which MCS actively targeted the tangent point of a solar occultation measurement by NOMAD.

Water vapor retrievals from NOMAD SO measurements were already presented in Aoki et al. (2019), covering the GDS and the late-season large-scale regional dust storm (“C” storm, Kass et al., 2016) of MY34 from April 21, 2018 ($L_s = 163^\circ$) to February 23, 2019 ($L_s = 345^\circ$). For this study, a revised version of the retrieval was used that included an updated NOMAD calibration, and the database was extended until March 7, 2019 ($L_s = 352^\circ$). We search iteratively for coordinated MCS measurements that fall within a time and space window centered on each

NOMAD measurement. We chose to pick MCS measurements that are within (1) ± 1 h in UTC time, (2) ± 1 h in local time, (3) $\pm 15^\circ$ in longitude, and (4) $\pm 5^\circ$ in latitude. For the serendipitous co-located observations during the GDS the latitude criterion was reduced to $\pm 3^\circ$ due to the highly dynamic meteorological situation and because the identified observations were located close to the edge of the northern polar vortex. We focus on seven families of coordinated measurements between NOMAD and MCS. Table 2 and Fig. 2 summarize every MCS and NOMAD family of measurements that were taken into account in this intercomparison study. Families 1 to 4 cover a latitude band in the northern high latitudes during the decay phase of the MY34 global dust event (Kleinböhl et al., 2020). They comprise of one NOMAD measurement each, surrounded by a sequence of nearly-continuous MCS measurements. Families 5 to 7 cover three latitude bands in the southern high latitudes after the late-season regional dust event in that Mars Year.

Fig. 3 shows individual profiles of MCS atmospheric temperature, MCS dust extinction, MCS water ice extinction and NOMAD water vapor VMR for the families of coordinated measurements described in Table 2. Temperature profiles in families 1 to 4 show the influence of the GDS, with temperatures approaching 210 K around 30 km and temperature

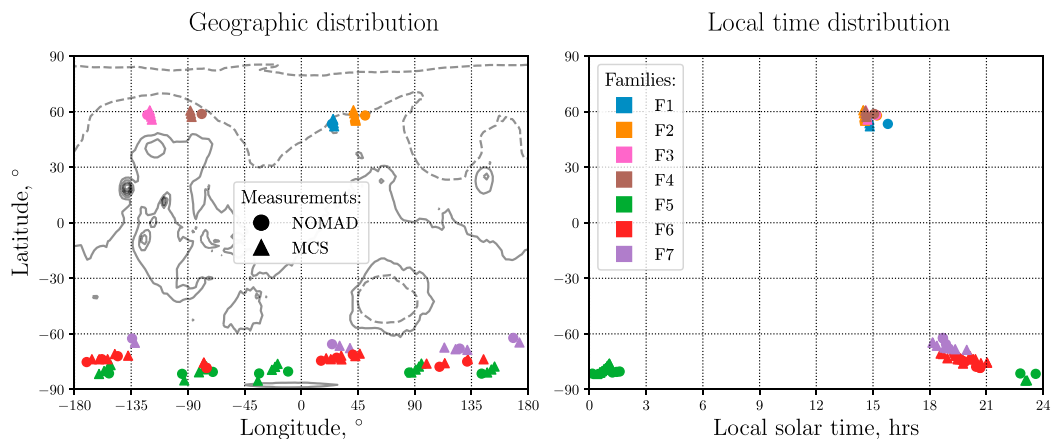


Fig. 2. Geographic distribution (left) and local time distribution vs. latitude (right) of co-located observations between NOMAD (circles) and MCS (triangles). Measurements have been divided in seven different families according to Table 2, with families 1 to 4 covering the Global dust event of MY34 ($L_s \in [241.1^\circ, 244.7^\circ]$), and families 5 to 7 covering the southern high latitude summer ($L_s \in [338.9^\circ, 347.3^\circ]$).

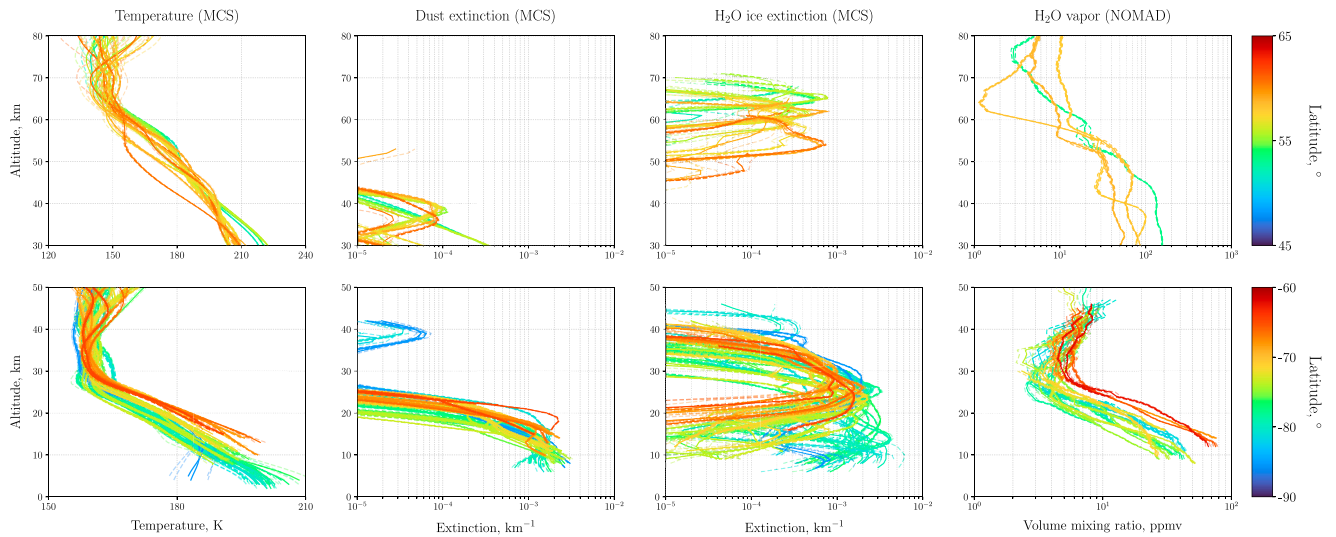


Fig. 3. Individual profiles of atmospheric temperature from MCS (left), dust extinction from MCS (center left), water ice extinction from MCS (center right) and water vapor mixing ratio from NOMAD (right) from coordinated measurements of families 1 to 4 (top) as well as families 5 to 7 (bottom) as provided in Table 2. Error bars (dotted lines) correspond to the precision of the individual measurements.

minima located between 60 and 70 km altitude. Dust is largely confined to altitudes below 40 km due to the high latitude, while water ice cloud opacities peak around 60 km altitude. NOMAD water vapor mixing ratios show a distinct rapid decrease between 50 and 60 km altitude, while the profiles above and below this altitude range vary much more slowly with altitude. Temperature and dust content in families 5–7 are much lower in the lower atmosphere compared to families 1–4 and show seasonal behavior, with temperatures between 60°S and 70°S being slightly warmer than further poleward. Temperatures decrease up to about 30 km altitude, stay almost constant for about 10 km, and start increasing slowly above that. Dust is mostly confined below 30 km altitude and shows a

3.2. Calculations

3.2.1. Saturated water vapor

Although MCS does not directly measure water vapor itself, the limb-viewing retrievals of temperature, pressure, ice and dust extinctions can be used to estimate water vapor assuming conditions of saturation (Heavens et al., 2018).

Pressure P and temperature T on Mars do not allow for the existence of liquid water in the martian atmosphere, so we use the formula describing water vapor pressure over ice P_{sat} as a function of temperature by Murphy and Koop (2005)

$$P_{sat}(T) = \exp\left(9.550426 - \frac{5723.265}{T} + 3.53068 \cdot \ln(T) - 0.00728332 \cdot T\right), \quad T \in [110 \text{ K}, 273.15 \text{ K}] \quad (1)$$

very steep falloff. Water ice is largely located above the dust layer, with opacities peaking between 20 and 30 km altitude. Profiles at high southern latitudes show additional opacity between 10 and 20 km altitude. NOMAD water vapor VMRs show a decrease from about 100 ppm around 10 km to less than 10 ppm around 30 km, followed by slow increase again towards higher altitudes.

NOMAD data are provided as individual profiles between –20 and 120 km altitude above the areoid (each cell being 1 km tall). Each individual MCS pressure, temperature, dust extinction and water ice extinction profile is first used to estimate MCS total atmospheric density as $\rho_{tot} = \frac{P}{k_B T}$ and water vapor VMR at saturation above the areoid (see Methods). Each group of MCS total atmospheric density profiles collocated around a single individual NOMAD water vapor number density profile (ρ_{H_2O}) is averaged into one MCS total atmospheric density profile in order to recalculate the individual NOMAD water vapor VMR profile as $\mu_{H_2O} = \frac{\rho_{H_2O}}{\rho_{tot}}$. Finally MCS data are interpolated to match NOMAD vertical grid.

We use this formula over the original Goff-Gratch equation (Goff, 1957, 1965) because it fits a wider range of temperatures suitable for the entire martian atmosphere. We calculate saturated water vapor content as $\frac{P_{sat}(T)}{P}$. We estimate water vapor in the presence of cloud ice, at every point of an atmospheric profile that satisfies the following conditions (Heavens et al., 2018): (1) water ice extinction $> 10^{-4} \text{ km}^{-1}$, and (2) water ice extinction $>$ dust extinction. In addition, we extend the estimation to every point within 10 km (about one scale height) above the cloud in order to investigate the processes that involve cloud nucleation and sedimentation. The right panels of Fig. 1 show calculations of saturated water vapor for two daytime half-orbits of MCS measurements coordinated with CRISM in parts of the atmosphere that fulfill these conditions.

3.2.2. Saturation ratio

The saturation ratio S is calculated as the ratio of the ambient water vapor VMR μ_{H_2O} over the saturated water vapor VMR μ_{sat}

$$S = \frac{\mu_{\text{H}_2\text{O}}}{\mu_{\text{sat}}} \quad (2)$$

In the case of the NOMAD study, we propagate the standard errors $\sigma_{\mu_{\text{H}_2\text{O}}}$ and $\sigma_{\mu_{\text{sat}}}$ of the two VMRs so that the error in the saturation ratio is defined as

$$\begin{aligned} \sigma_S &= \sqrt{\left(\frac{\partial S}{\partial \mu_{\text{H}_2\text{O}}}\right)^2 \cdot \sigma_{\mu_{\text{H}_2\text{O}}}^2 + \left(\frac{\partial S}{\partial \mu_{\text{sat}}}\right)^2 \cdot \sigma_{\mu_{\text{sat}}}^2} \\ &= \sqrt{\left(\frac{1}{\mu_{\text{sat}}}\right)^2 \cdot \sigma_{\mu_{\text{H}_2\text{O}}}^2 + \left(-\frac{\mu_{\text{H}_2\text{O}}}{\mu_{\text{sat}}^2}\right)^2 \cdot \sigma_{\mu_{\text{sat}}}^2}. \end{aligned} \quad (3)$$

4. Results

4.1. MCS and CRISM

The CRISM part of the study allows us to evaluate the saturation state of the atmosphere and its variation with season. We separate the clear and dusty seasons into the two following L_s ranges: $L_s \in [30^\circ, 140^\circ]$ and $L_s \in [140^\circ, 360^\circ]$. Transects of MCS saturated water vapor VMR are

averaged using an arithmetic mean within each bin of the zonal grid for six periods of L_s covering the following subsets of the martian year, corresponding to Tables 2–7 in Clancy et al. (2017): $L_s \in [30^\circ, 60^\circ]$, $L_s \in [60^\circ, 100^\circ]$, $L_s \in [100^\circ, 140^\circ]$, $L_s \in [140^\circ, 200^\circ]$, $L_s \in [200^\circ, 310^\circ]$, and $L_s \in [320^\circ, 360^\circ]$.

As described in the Methods section, we apply saturated water vapor estimates following a set of conditions that identify cloud occurrence, and then extend these estimates 10 km above the top of the cloud. In order to track cloud occurrence, we first calculate the ratio of measurement points estimated to be in the presence of clouds for each latitude-altitude bin. The first column in Fig. 4 shows the fraction of this number to the total number of measurements, indicating regions of the atmosphere where water ice clouds exist in red (between 0.6 and 1), regions above the clouds in blue (between 0 and 0.4) and at the top of the cloud the transition between the two is in white (between 0.4 and 0.6) for the six periods of L_s covering the martian year.

Columns 2 and 3 in Fig. 4 show zonal averages of MCS saturated water vapor mixing ratio in comparison with CRISM water vapor mixing ratio. In the clear season a good correspondence of the overall morphology of the water vapor distribution in the two datasets can be

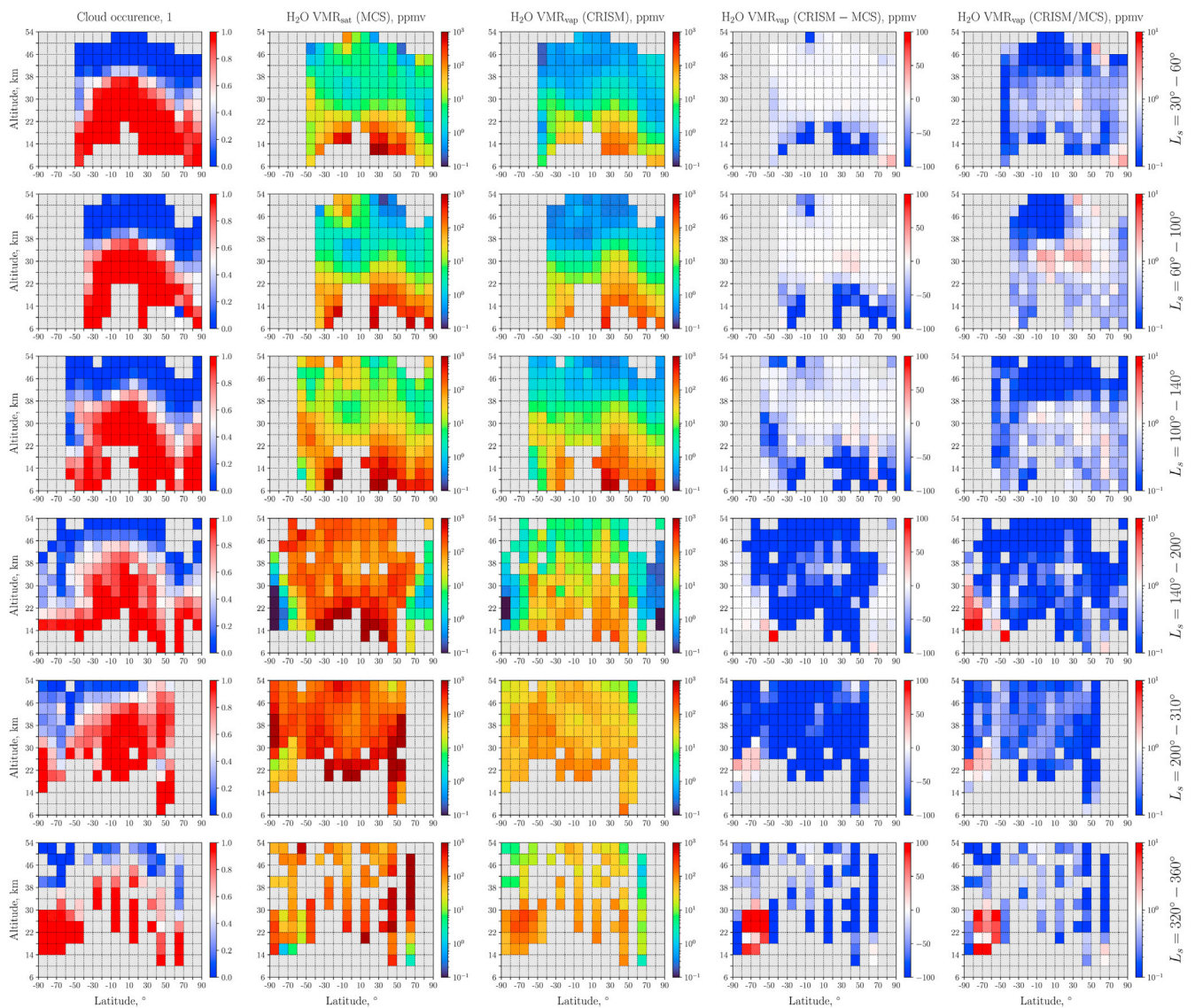


Fig. 4. Ratio of measurement points with cloud occurrence to total number of measurement points for MCS (far left), and zonal averages of saturated water vapor mixing ratio derived from MCS (center left), ambient water vapor mixing ratio derived from CRISM (center), difference in water vapor mixing ratio between CRISM and MCS (center right) and saturation ratio (far right) for six periods of L_s covering the martian year.

observed. At altitudes above the clouds, MCS zonal averages reveal small patches of increased saturated water vapor at low southern latitudes that are not present in CRISM zonal averages. The dusty season is characterized by a rise of the hygro-pause, with the region of cloud occurrence almost reaching the top of the considered altitude range. Higher atmospheric temperatures lead to an increase in MCS saturated water vapor, which tends to be somewhat higher than the CRISM zonal averages. Little latitudinal structure is observed in the water vapor distributions of both instruments at mid- and low latitudes in this season. Only at high latitudes some decrease in water vapor mixing ratio is observed, in particular at $L_s \in [140^\circ, 200^\circ]$, when both polar regions are influenced by polar vortices (McCleese et al., 2010).

The last two columns in Fig. 4 allow us to study the difference in water vapor mixing ratio and the saturation ratio based on MCS and CRISM zonal averages. In the aphelion season CRISM ambient water vapor is usually near saturation or slightly supersaturated in the presence of clouds. Supersaturation reaches a factor of 1.4 for $L_s \in [30^\circ, 60^\circ]$, a factor of 2.5 for $L_s \in [60^\circ, 100^\circ]$, and a factor of 1.3 for $L_s \in [100^\circ, 140^\circ]$. Subsaturated conditions appear to be indicated above and below the primary ACB formation region of $\sim 20\text{--}40$ km over this aphelion period, with low to mid-latitude concentrations that correspond coarsely to the ACB latitudinal extent.

During the dustier perihelion season the atmosphere appears largely

subsaturated for each period of L_s . Some supersaturation is only suggested in a region close to the south pole between 14 and 34 km ($90^\circ\text{S} - 60^\circ\text{S}$). However, for $L_s \in [140^\circ, 200^\circ]$ the water vapor values are very small in both the MCS and CRISM zonal averages due to the cold temperatures in the decaying polar vortex, and the absolute difference in mixing ratio is close to zero. In the other L_s -ranges of the dusty season, temperatures and water vapor mixing ratios in the southern high latitudes are somewhat higher but still suggest some level of supersaturation.

Fig. 5 shows correlations between saturated water vapor mixing ratio from MCS and ambient water vapor mixing ratio from CRISM for six periods of L_s covering the martian year. Correlations are calculated from each latitude-altitude bin of the MCS and CRISM water vapor zonal averages. Following Clancy et al. (2017), CRISM error bars are displayed assuming a 30% error in CRISM water vapor below 20 km and a 20% error in CRISM water vapor above 20 km. MCS error bars are computed assuming a 3 K accuracy of the underlying MCS temperatures. The saturation state of the atmosphere within a bin can be described by the position of the point relative to the diagonal line going from the origin out to high x-and-y-values: (1) points above the line represent bins where the ambient water vapor is subsaturated, (2) points on the line represent bins where the ambient water vapor is saturated, and (3) points below the line represent bins where the ambient water vapor is supersaturated.

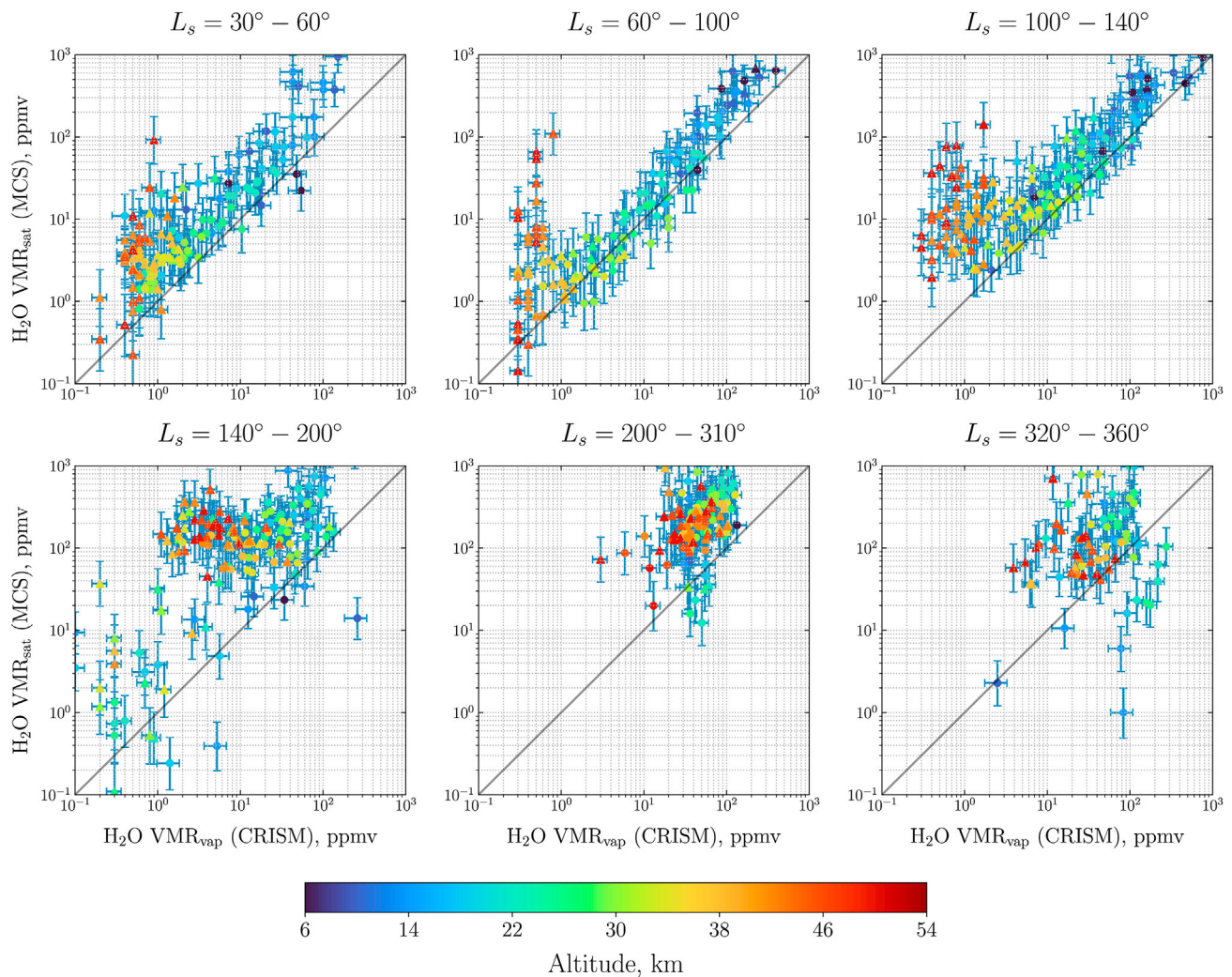


Fig. 5. Correlations between saturated water vapor mixing ratio from MCS and ambient water vapor mixing ratio from CRISM. Colors indicate the altitude the data point corresponds to. Horizontal error bars correspond to a 30% error in CRISM water vapor below 20 km and a 20% error in CRISM water vapor above 20 km while vertical error bars in water vapor are derived assuming a 3 K accuracy (± 3 K variation centered on the presented temperature) of the underlying MCS temperatures. Bins with cloud occurrences above 50% are represented by circles, while bins with cloud occurrences below this threshold are represented by triangles.

Circle-shaped points indicate data with 50% or more cloud occurrence, whereas triangle-shaped points show data with less than 50% cloud occurrence.

The correlations derived from MCS and CRISM zonal averages allow us to appreciate the real extent of the agreement during the aphelion season: we observe for each period of L_s a high positive correlation in cases with cloud occurrence (circle-shaped points). The cloud of circle-shaped points is shifted slightly upwards from the middle line which means that most bins are slightly subsaturated, while the rest of the bins are either at saturation or slightly supersaturated. Points at altitudes above the clouds (triangle-shaped points) significantly deviate from the one-to-one line in the correlation. Most of them are shifted upwards, well into the subsaturated region of the diagram, although we do observe some saturated data points above the cloud in the northern hemisphere

for $L_s \in [60^\circ, 100^\circ]$. We note that the recently reported discussion of a potential bias in Mars photochemistry by Lefèvre et al. (2021) would shift CRISM-derived water values to the right by $\sim 30\%$, leading to somewhat closer agreement with saturated conditions overall. In the dusty season ($L_s \in [140^\circ, 360^\circ]$), MCS-CRISM inferred saturation ratios predominantly fall within the subsaturated portions of the diagrams in Fig. 5. Only few data points, typically at altitudes between 15 and 30 km, overlap with the saturation line. Data points with low water vapor mixing ratios scattered around the saturation line at $L_s \in [140^\circ, 200^\circ]$ largely correspond to measurements in the polar regions where temperatures are very cold at this season. Supersaturated data points at $L_s \in [320^\circ, 360^\circ]$ also correspond to the south polar region.

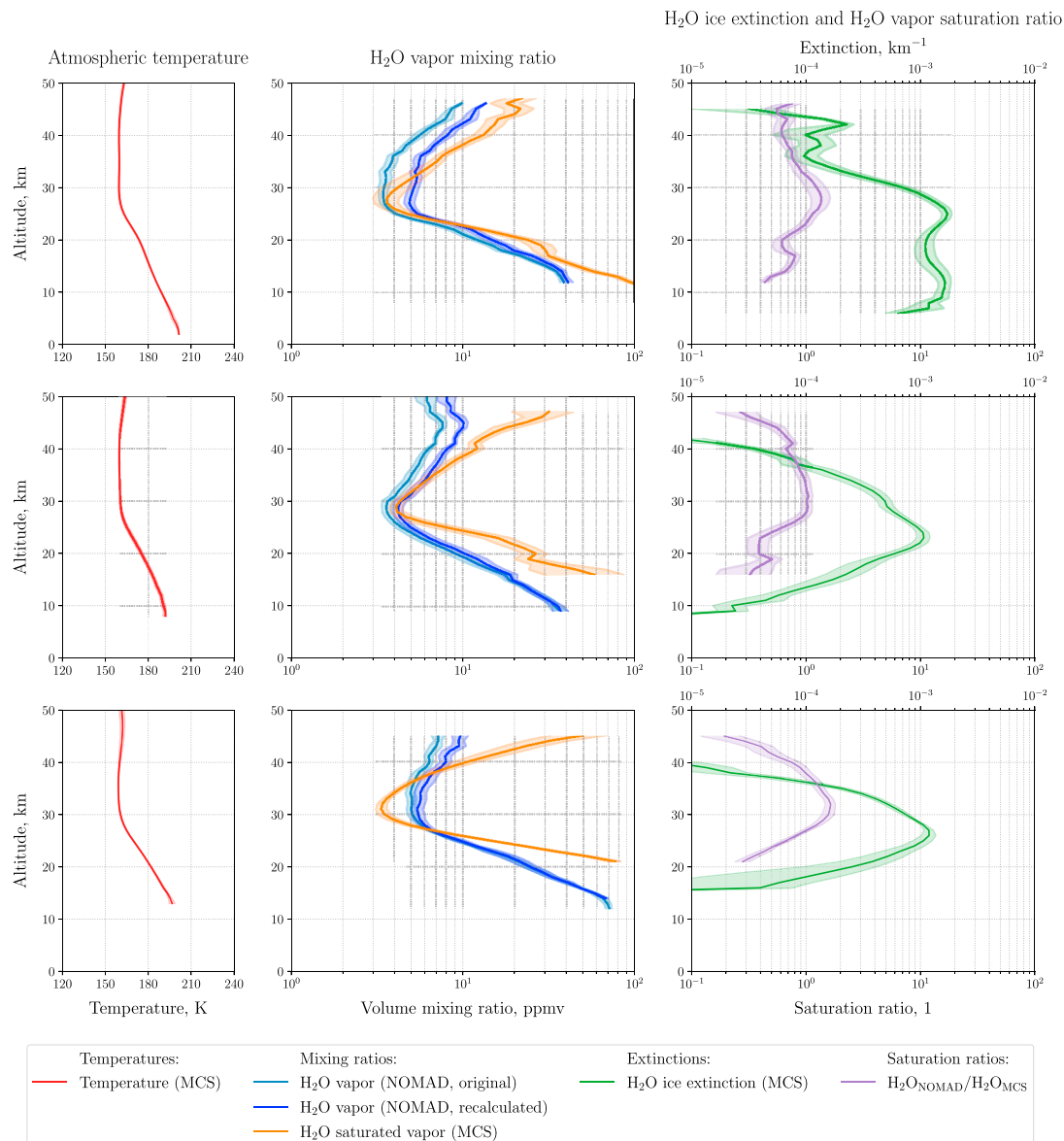


Fig. 6. Average profiles of temperature, water vapor, water ice opacity, and water saturation ratio for three southern high latitude bands in southern summer (families 5, 6 and 7, $L_s \in [338.9^\circ, 347.3^\circ]$). Left: Atmospheric temperature profiles from MCS. Center: Water vapor mixing ratio profiles from NOMAD (light blue), recalculated using MCS temperatures and pressures (dark blue), and saturated mixing ratio profiles based on MCS temperatures (orange). Right: Water ice opacity from MCS (green) and saturated mixing ratio (purple). Shaded areas give the standard error.

4.2. MCS and NOMAD

The NOMAD part of the study allows us to evaluate the saturation state of the atmosphere during the dusty season in detail. We separate the dataset into seven families of measurements retrieved during the decay phase of the MY34 GDS (around $L_s = 240^\circ$) and after the MY34 C storm (around $L_s = 340^\circ$). For each family of MCS temperature, MCS water ice extinction, MCS saturated water vapor VMR, as well as for NOMAD ambient water vapor VMR in families 5–7, profiles are averaged using an arithmetic mean on a 1 km vertical the grid (see Table 2). The standard error for the averages is also computed (see Methods). The saturation ratio is derived from the averages using equation (2), with its uncertainty derived through error propagation

using equation (3).

Fig. 6 shows a side-by-side comparison between MCS and NOMAD vertical profile averages of temperature, water vapor, water ice opacity, and water vapor saturation ratio for three southern high latitude bands in southern summer after the MY34 C storm ($L_s \in [338^\circ, 348^\circ]$). At this season and latitude, temperature decreases between 10 and 30 km altitude until it reaches a minimum between 30 and 40 km altitude. We observe that NOMAD ambient water vapor in families 5, 6 and 7 is often close to saturation in the presence of water ice clouds between 10 and 40 km, with the ambient water vapor mixing ratio following the saturated mixing ratio over a large vertical extent. Some supersaturation occurs in the profiles of family 7 around 30 km altitude, slightly above the peak in ice opacity, but it does not reach a factor of 2. For the other two families

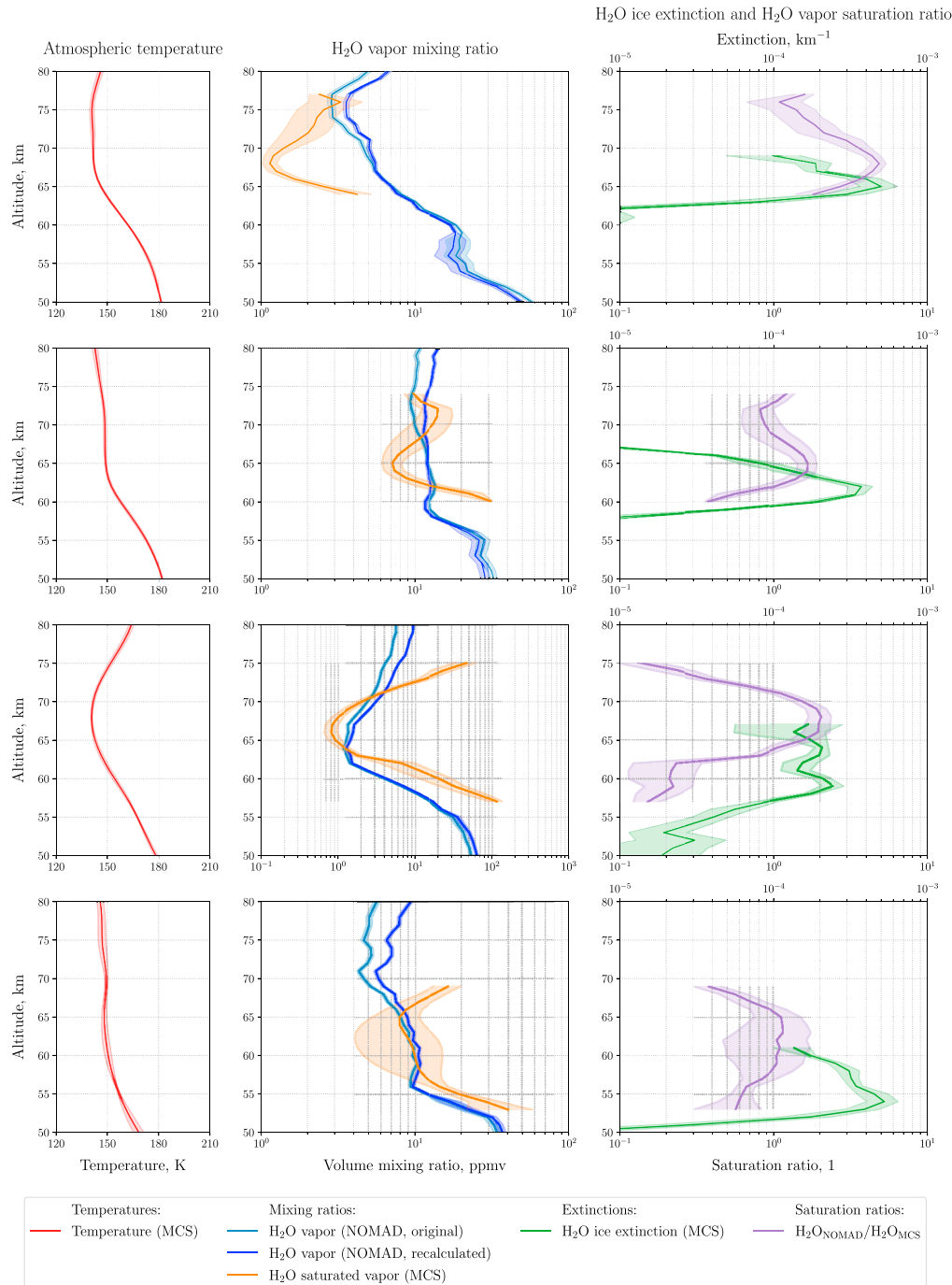


Fig. 7. As in Fig. 6 but for four northern mid-latitude locations during the Global Dust Event of MY34 (families 1 to 4, $L_s \in [241.1^\circ, 244.7^\circ]$).

the atmosphere is close to saturation over a significant vertical range. For all families some subsaturation towards the bottom of the cloud is observed where water ice is still present. Above the top of the cloud, the atmosphere is also largely subsaturated as temperature increases slightly above 40 km altitude, suggesting that extended regions of supersaturation are not required to form clouds.

Fig. 7 shows side-by-side comparisons between MCS and NOMAD vertical profiles of temperature, water vapor, water ice opacity, and water vapor saturation ratio for four northern high latitude locations during the decay phase of the MY34 GDS ($L_s \in [241^\circ, 245^\circ]$). During the decay phase of the GDS the atmosphere is more dynamic and MCS observes that water ice clouds in families 1 to 4 reach higher altitudes between 50 and 70 km. Temperature decreases between 50 and 60 km altitude until it reaches a minimum between 60 and 70 km altitude. Supersaturation occurs in a roughly 10 km wide vertical range in family 1 and a ~ 5 km wide vertical range in families 2 and 3. The saturation profile of family 4 is close to a saturation ratio of 1 over a nearly 10 km wide vertical range. The maximum supersaturation is observed in family 1, where a supersaturation ratio of about 5 is reached. In families 2 and 3 the supersaturation ratio does not exceed 2. In families 1–3 the maximum supersaturation is reached a few km above the peak of the cloud opacity, similar to the structure found at high southern latitudes (see Fig. 6). The atmosphere rapidly reaches a state of subsaturation below the saturated or supersaturated regions of the atmosphere at the bottom of the clouds for all families. Above the top of the clouds, we observe a rapid drop in saturation ratio from supersaturation to subsaturation around 70 km for families 3 and 4. The overall behavior of the examples in Fig. 7 suggests that also in these conditions, extended regions of supersaturation are not required to form clouds.

5. Discussion

Our results based on both the CRISM and NOMAD studies do not find evidence for large or widespread supersaturation in the martian atmosphere. The CRISM analysis shows the saturation state of the atmosphere in an average sense and its variation with season: during the clear season the atmosphere is close to saturation when clouds are present and can reach supersaturation with no more than 2 to 3 times the amount of saturated water vapor in the altitude range studied ($\sim 10 - 50$ km). This supersaturation is most prominent at $L_s \in [60^\circ, 100^\circ]$ at mid- and low latitudes around 30 km altitude near the top of the cloud layer. This is consistent with findings that compare water vapor derived from CRISM with saturated water vapor from model-derived temperatures, where supersaturations of factors up to about 3 were derived in the aphelion cloud belt ($L_s \in [60^\circ, 140^\circ]$) near the top of the cloud layer (30 – 40 km altitude), while altitudes below were near saturation or slightly subsaturated (Clancy et al., 2017). Above the clouds (~ 40 km altitude) the atmosphere is largely subsaturated, indicating that large supersaturations are not required to form water ice clouds.

During the dusty season subsaturation is more prevalent than supersaturation based on the CRISM analysis. The comparison with CRISM shows a lack of supersaturation in mid- and low latitudes in averages during the dusty season, which again is consistent with comparisons involving saturated water vapor from model-derived temperatures at $L_s \in [200^\circ, 310^\circ]$ (Clancy et al., 2017). We note that narrow layers of supersaturation might not be resolved in this analysis as the data for the CRISM comparisons are binned over 4 km and averages over multiple orbits had to be created to improve signal-to-noise (Clancy et al., 2017). In addition, the atmosphere is more dynamic in the dusty season than in the clear season, and dust storms occurrences can lead to varying hygropause altitudes, such that narrow layers of supersaturation might not appear in zonal averages over large ranges of L_s . If the recently suggested potential bias in Mars photochemistry (Lefevre et al., 2021) was considered, the results from the CRISM study would fall closer to average saturated conditions for the aphelion season in particular.

The NOMAD analysis shows the average saturation state of a few

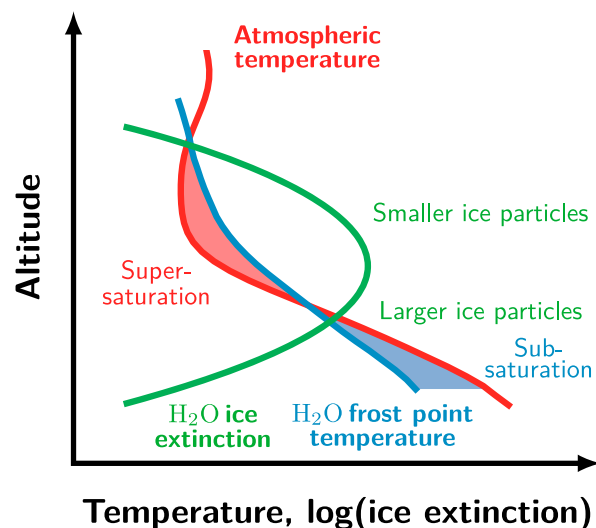


Fig. 8. Schematic summarizing the saturation state of the atmosphere in the presence of cloud occurrence and the evolution of water ice particles. Red, blue and green lines represent the atmospheric temperature, the water vapor frost point temperature and the logarithm of water ice extinction, respectively. The region of supersaturation is shaded red while the region of subsaturation is shaded blue.

southern high latitude bands of the atmosphere following the C storm of MY34 and suggests the atmosphere is close to saturation when clouds are present, with possibly a supersaturated layer confined to a small vertical range above the peak of the cloud opacity. During the decay phase of the GDS, where individual NOMAD water profiles at mid-to high northern latitudes are compared with narrow latitudinal averages of MCS profiles, clouds shift higher up but the overall structure is still comparable, with saturated or supersaturated regions towards the top and subsaturated regions towards the bottom of cloud layers. In these examples the supersaturation ratios reached nearly 5 in one case but did not exceed 2 in the other cases.

We propose a schematic model of cloud formation and evolution in Fig. 8 that illustrates a qualitative explanation regarding the saturation state of the atmosphere in the presence and proximity of cloud occurrence as observed by MCS, NOMAD and CRISM. When the atmospheric temperature drops below the frost point at high altitudes, small water ice particles start to form. No large supersaturations are required for this to happen, suggesting that cloud condensation nuclei, most likely in the form of small dust particles, are sufficiently abundant to enable nucleation. The water ice particles grow in size due to constant exposition to water vapor on their surfaces in conditions of saturation or supersaturation and through coagulation by colliding with other ice particles. As they grow the particles will fall due to gravity while consuming the available water vapor on their way through the atmosphere. The suggested structure in ice particle size is qualitatively consistent with recent results by Luginin et al. (2020), who found a general trend of decreasing ice particle size with altitude. As the particles reach warmer and more subsaturated regions of the atmosphere, they start to sublimate. Hence the condition of subsaturation at the bottom of water ice clouds is likely related to ice particles falling into these subsaturated regions and evaporating. The proposed mechanism is consistent with ubiquitous observations of water ice clouds around local temperature minima caused by the diurnal tide in the martian atmosphere, where maxima in water ice opacity are typically located at slightly lower altitudes than the corresponding temperature minima (Lee et al., 2009). It is also qualitatively consistent with recent findings by Guzewich and Smith (2019), who report that low-latitude water ice clouds exhibit particle size sorting with altitude at all seasons, and is more in line with a traditional view of cloud formation (Daerden et al., 2010). The proposed process has similarities to

the formation and evolution of Polar Mesospheric Clouds on Earth, where water ice particles form around temperature minima created in the ascending branch of the mesospheric circulation in the summer polar mesopause region, and grow and subsequently sediment to lower altitudes (Rapp and Thomas, 2006, compare their Fig. 1).

Maltagliati et al. (2011) investigated the saturation of the atmosphere during northern spring and summer ($L_s \in [50^\circ, 110^\circ]$) of MY29 using SPICAM observations of water vapor in mid-to high latitudes in comparison with temperatures modeled by the LMDGCM. Most profiles indicated some level of supersaturation, with peak supersaturation ratios between 2 and 5 in the southern and between 2 and 10 in the northern hemisphere around 30–40 km altitude and some northern hemispheric profiles exhibiting supersaturation up to ~ 50 km altitude. At altitudes below 20–30 km the supersaturation typically turns to subsaturation. These estimates were not calculated as a function of water ice cloud occurrence but given the widespread cloud occurrence during this season (Lee et al., 2009; Heavens et al., 2010, this work) some cloud occurrence is likely to be expected. While the supersaturations derived by Maltagliati et al. (2011) are larger in magnitude than the ones obtained in this work, the altitude range in which supersaturation occurs roughly corresponds to regions of light supersaturation from comparisons with CRISM in the same season (second row of Fig. 4). Maltagliati et al. (2011) suggest that the scavenging effect, the removal of dust particles from the atmosphere captured by falling water ice particles leading to a lack of condensation nuclei, was the main mechanism behind the supersaturation levels observed by SPICAM. While the widespread cloud occurrence at this season might draw the importance of the scavenging effect into question, the process of ice particle formation and sedimentation outlined in this work is qualitatively consistent with the overall transition of supersaturation to subsaturation at altitudes around 20 km reported by Maltagliati et al. (2011). In a follow-on study Maltagliati et al. (2013) extended their analysis to the dusty season ($L_s \in [205^\circ, 275^\circ]$) and did not find any supersaturation except in one profile at high altitudes. This is largely consistent with our results from this work considering that we found only narrow layers of supersaturation up to factors of 2–5 in comparisons with NOMAD.

More recently the ACS instrument suite on ExoMars TGO retrieved temperatures and water vapor mixing ratios during the southern spring and summer ($L_s \in [160^\circ, 360^\circ]$) that suggest very high levels of supersaturation even in the presence of aerosols (Fedorova et al., 2020). Saturation ratios frequently exceeded 10 at altitudes above 40–50 km in the decay phases of the global and C regional storms of that Mars Year, with saturation ratios even exceeding 100 between 80 and 90 km altitude during the main phase of the GDS. High supersaturations were also found at altitudes below 40 km in southern high latitudes prior to the onset of the global and C regional storms as well as after the C storm, and additionally at northern high latitudes around the equinoxes. Our results from the comparisons of MCS saturated water with NOMAD ambient water suggest that the average supersaturation at high southern latitudes after the C storm is rather modest, not exceeding 2, while ambient water vapor is close to saturation over large ranges of altitude. In the examples shown for the decay phase of the GDS at mid-to high northern latitudes the comparisons of MCS saturated water with NOMAD ambient water also suggest rather modest supersaturation towards the top of cloud layers that formed above the bulk of the dust, with water vapor mixing ratios quickly reaching subsaturated regimes below. Our results do not exclude large supersaturations at higher altitudes or lower latitudes, as presented by Fedorova et al. (2020). We also point out that the atmosphere during the GDS was highly dynamic, with large lateral variations in both temperature and water vapor that could affect the saturation state of the atmosphere at small scales. However, our findings are more in line with the traditional understanding that water vapor in the presence of water ice clouds is near saturation, and that strong supersaturation is not required to form clouds in the martian atmosphere (Daerden et al., 2010). Comparisons of MCS saturated water vapor with water vapor derived from CRISM in the southern high latitudes do suggest some

supersaturation at low altitudes in the dusty season. However, we note that at least around the equinoxes the atmosphere in this region is influenced by the polar vortex (McCleese et al., 2010), where lateral gradients can impact limb measurements (Kleinböhl et al., 2017b) as well as solar occultation measurements, which also have long lightpaths through the atmosphere. Future coordinated measurements between MCS and NOMAD as well as ACS, in addition to detailed intercomparisons between water vapor profiles from the NOMAD and ACS instruments themselves, will help to further constrain the saturation state of the martian atmosphere.

6. Conclusions

We have evaluated water vapor saturation in the martian atmosphere in the presence or proximity of water ice clouds by comparing profile averages of ambient water vapor derived from CRISM and NOMAD measurements with profile averages of saturated water derived from MCS temperature profiles. We come to the following conclusions:

- During the aphelion season the atmosphere is close to saturation in the presence of clouds. Supersaturation ratios reach values of no more than 2 to 3 towards the top of the cloud layer.
- During the perihelion season water vapor is close to saturation or somewhat subsaturated in the presence of clouds, with some supersaturation towards the top of the clouds. Regions towards the bottom of the clouds are often subsaturated.
- Based on the examples studied during the Global Dust Storm the region of cloud occurrence shifts to higher altitudes but the overall structure of supersaturated vs. subsaturated regions does not change markedly.
- The atmosphere above cloud layers appears largely subsaturated, suggesting that cloud formation is fairly instantaneous upon the temperature dropping below the frost point. Large amounts of supersaturation are not required to form water ice clouds.
- We propose a schematic model of cloud evolution in which small cloud particles are formed rapidly as the temperature drops below the frost point, leading to water vapor being saturated or slightly supersaturated. As particles fall they grow through additional vapor deposition and coagulation, until they reach subsaturated regions of the atmosphere. This model would be consistent with the atmosphere being slightly supersaturated towards the top but subsaturated towards the bottom of a cloud layer.

We suggest future coordinated measurements between MCS and the solar occultation instruments on ExoMars TGO as well as extended intercomparisons between the TGO instruments in order to further constrain the saturation state of the martian atmosphere.

Author statement

All authors have seen and approved the final version of the manuscript. They warrant that the article is the authors' original work, hasn't received prior publication and isn't under consideration for publication elsewhere.

Declaration of competing interest

The authors declare that they have no known competing financial interests or personal relationships that could have appeared to influence the work reported in this paper.

Acknowledgments

We thank Frank Daerden for fruitful discussions and helpful suggestions on the manuscript. L. P. is grateful for a grant from ESTACA, allowing him to participate in a remote internship at JPL via the JPL

Visiting Student Research Program. A. K. acknowledges support from the Mars Data Analysis Program (80NM0018F0719). We thank the MCS instrument and MRO spacecraft operations teams for making the coordinated observations with the CRISM and NOMAD instruments possible. Work at the Jet Propulsion Laboratory, California Institute of Technology, is performed under contract with the National Aeronautics and Space Administration. Copyright 2021, California Institute of Technology. All rights reserved.

References

- Aoki, S., Vandaele, A., Daerden, F., Villanueva, G., Liuzzi, G., Thomas, I., Erwin, J., Trompet, L., Robert, S., Neary, L., et al., 2019. Water vapor vertical profiles on Mars in dust storms observed by TGO/NOMAD. *J. Geophys. Res.* 124 (12), 3482–3497. <https://doi.org/10.1029/2019JE006109>.
- Chaffin, M.S., Deighan, J., Schneider, N.M., Stewart, A.I.F., 2017. Elevated atmospheric escape of atomic hydrogen from Mars induced by high-altitude water. *Nat. Geosci.* 10 (3), 174–178. <https://doi.org/10.1038/ngeo2887>.
- Chaffin, M.S., Kass, D.M., Aoki, S., Fedorova, A.A., Deighan, J., Connour, K., Heavens, N.G., Kleinböhl, A., Jain, S.K., Chaufray, J.-Y., Mayyasi, M., Clarke, J.T., Stewart, A.I.F., Evans, J.S., Stevens, M.H., McClintock, W.E., Crismani, M., Holsclaw, G.M., Lefevre, F., Lo, D.Y., Montmessin, F., Schneider, N.M., Jakosky, B., Villanueva, G., Liuzzi, G., Daerden, F., Thomas, I.R., Lopez-Moreno, J.-J., Patel, M.R., Bellucci, G., Ristic, B., Erwin, J.T., Vandaele, A.C., Trokhimovskii, A., Korablev, O.I., 2021. Martian water loss to space enhanced by regional dust storms. *Nat. Astron.* 5 (10), 1036–1042. <https://doi.org/10.1038/s41550-021-01425-w>.
- Clancy, R.T., Grossman, A.W., Wolff, M.J., James, P.B., Rudy, D.J., Billawala, Y.N., Sandor, B.J., Lee, S.W., Muhleman, D.O., 1996. Water vapor saturation at low altitudes around Mars aphelion: a key to Mars climate? *Icarus* 122 (1), 36–62. <https://doi.org/10.1006/icar.1996.0108>.
- Clancy, R.T., Sandor, B.J., García-Muñoz, A., Lefevre, F., Smith, M.D., Wolff, M.J., Montmessin, F., Murchie, S.L., Nair, 2013. First detection of Mars atmospheric hydroxyl: CRISM near-IR measurement versus LMD GCM simulation of OH Meinel band emission in the Mars polar winter atmosphere. *Icarus* 226, 272–281. <https://doi.org/10.1016/j.icarus.2013.05.035>.
- Clancy, R.T., Sandor, B.J., Wolff, M.J., Smith, M.D., Lefevre, F., Madeleine, J.-B., Forget, F., Murchie, S.L., Seelos, F.P., Seelos, K.D., Nair, H.A., Toigo, A.D., Humm, D., Kass, D.M., Kleinböhl, A., Heavens, N., 2012. Extensive MRO CRISM observations of 1.27 μm O₂ airglow in Mars polar night and their comparison to MRO MCS temperature profiles and LMD GCM simulations. *J. Geophys. Res.* 117 (E11), e00J10. <https://doi.org/10.1029/2011JE004018>.
- Clancy, R.T., Smith, M.D., Lefevre, F., Mcconnochie, T.H., Sandor, B.J., Wolff, M.J., Lee, S.W., Murchie, S.L., Toigo, A.D., Nair, H., et al., 2017. Vertical profiles of Mars 1.27 μm O₂ dayglow from MRO CRISM limb spectra: seasonal/global behaviors, comparisons to LMD GCM simulations, and a global definition for Mars water vapor profiles. *Icarus* 293, 132–156. <https://doi.org/10.1016/j.icarus.2017.04.011>.
- Clancy, R.T., Wolff, M.J., Smith, M.D., Kleinböhl, A., Cantor, B.A., Murchie, S.L., Toigo, A.D., Seelos, K., Lefevre, F., Montmessin, F., Daerden, F., Sandor, B.J., 2019. The distribution, composition, and particle properties of Mars mesospheric aerosols: an analysis of CRISM visible/near-ir limb spectra with context from near-coincident MCS and MARCI observations. *Icarus* 328, 246–273. <https://doi.org/10.1016/j.icarus.2019.03.025>.
- Daerden, F., Whiteway, J.A., Davy, R., Verhoeven, C., Komguem, L., Dickinson, C., Taylor, P.A., Larsen, N., 2010. Simulating observed boundary layer clouds on Mars. *Geophys. Res. Lett.* 37, 104203. <https://doi.org/10.1029/2009GL041523>.
- Fedorova, A.A., Montmessin, F., Korablev, O., Luginin, M., Trokhimovskiy, A., Belyaev, D.A., Ignatiev, N.I., Lefevre, F., Alday, J., Irwin, P.G., et al., 2020. Stormy water on Mars: the distribution and saturation of atmospheric water during the dusty season. *Science* 367 (6475), 297–300. <https://doi.org/10.1126/science.aay9522>.
- Goff, J., 1957. Saturation pressure of water on the new kelvin scale. *Am. Soc. Heat. Vent. Eng. Trans.* 63, 347–354.
- Goff, J., 1965. Saturation pressure of water on the new kelvin scale. In: *Humidity and Moisture Measurement and Control in Science and Industry*, 3, pp. 289–292.
- Guzewich, S.D., Smith, M.D., 2019. Seasonal variation in Martian water ice cloud particle size. *J. Geophys. Res.* 124, 636–643. <https://doi.org/10.1029/2018JE005843>.
- Heavens, N.G., Benson, J.L., Kass, D.M., Kleinböhl, A., Abdou, W.A., McCleese, D.J., Richardson, M.I., Schofield, J.T., Shirley, J.H., Wolkenberg, P.M., 2010. Water ice clouds over the Martian tropics during northern summer. *Geophys. Res. Lett.* 37, L18202. <https://doi.org/10.1029/2010GL044610>.
- Heavens, N.G., Kleinböhl, A., Chaffin, M.S., Halekas, J.S., Kass, D.M., Hayne, P.O., McCleese, D.J., Piqueux, S., Shirley, J.H., Schofield, J.T., 2018. Hydrogen escape from Mars enhanced by deep convection in dust storms. *Nat. Astron.* 2 (2), 126–132. <https://doi.org/10.1038/s41550-017-0353-4>.
- Hinson, D.P., Asmar, S.W., Kahan, D.S., Akopian, V., Haberle, R.M., Spiga, A., Schofield, J.T., Kleinböhl, A., Abdou, W.A., Lewis, S.R., et al., 2014. Initial results from radio occultation measurements with the Mars Reconnaissance Orbiter: a nocturnal mixed layer in the tropics and comparisons with polar profiles from the Mars Climate Sounder. *Icarus* 243, 91–103. <https://doi.org/10.1016/j.icarus.2014.09.019>.
- Kass, D.M., Kleinböhl, A., McCleese, D.J., Schofield, J.T., Smith, M.D., 2016. Interannual similarity in the Martian atmosphere during the dust storm season. *Geophys. Res. Lett.* 43, 6111–6118. <https://doi.org/10.1002/2016GL068978>.
- Kleinböhl, A., Chen, L., Schofield, J.T., 2017a. Far infrared spectroscopic parameters of Mars atmospheric aerosols and their application to MCS retrievals in high aerosol conditions. In: *Sixth International Workshop on the Atmosphere of Mars*. Granada, Spain.
- Kleinböhl, A., Friedson, A.J., Schofield, J.T., 2017b. Two-dimensional radiative transfer for the retrieval of limb emission measurements in the martian atmosphere. *J. Quant. Spectrosc. Radiat. Transfer* 187, 511–522.
- Kleinböhl, A., Schofield, J.T., Abdou, W.A., Irwin, P.G.J., de Kok, R.J., 2011. A single-scattering approximation for infrared radiative transfer in limb geometry in the Martian atmosphere. *J. Quant. Spectrosc. Radiat. Transfer* 112, 1568–1580. <https://doi.org/10.1016/j.jqsrt.2011.03.006>.
- Kleinböhl, A., Schofield, J.T., Kass, D.M., Abdou, W.A., Backus, C.R., Sen, B., Shirley, J.H., McCleese, D.J., Lawson, W.G., Richardson, M.I., Taylor, F.W., Teanby, N.A., 2009. Mars Climate Sounder limb profile retrieval of atmospheric temperature, pressure, and dust and water ice opacity. *J. Geophys. Res.* 114, E10006. <https://doi.org/10.1029/2009JE003358>.
- Kleinböhl, A., Spiga, A., Kass, D.M., Shirley, J.H., Millour, E., Montabone, L., Forget, F., 2020. Diurnal variations of dust during the 2018 Global Dust Storm observed by the Mars Climate Sounder. *J. Geophys. Res.* 125, e2019JE006115. <https://doi.org/10.1029/2019JE006115>.
- Lee, C., Lawson, W.G., Richardson, M.I., Heavens, N.G., Kleinböhl, A., Banfield, D., McCleese, D.J., Zurek, R.W., Kass, D.M., Schofield, J.T., Leovy, C.B., Taylor, F.W., Toigo, A.D., 2009. Thermal tides in the Martian middle atmosphere as seen by the Mars Climate Sounder. *J. Geophys. Res.* 114, E03005. <https://doi.org/10.1029/2009JE003285>.
- Lefevre, F., Bertaux, J.-L., Clancy, R.T., Encrenaz, T., Fast, K., Forget, F., Lebonnois, S., Montmessin, F., Perrier, S., 2008. Heterogeneous chemistry in the atmosphere of Mars. *Nature* 454 (7207), 971–975. <https://doi.org/10.1038/nature07116>.
- Lefevre, F., Lebonnois, S., Montmessin, F., Forget, F., 2004. Three-dimensional modeling of ozone on Mars. *J. Geophys. Res.: Planets* 109 (E7), E07004. <https://doi.org/10.1029/2004JE002268>.
- Lefevre, F., Trokhimovskiy, A., Fedorova, A., Baggio, L., Lacombe, G., Määttänen, A., Bertaux, J.-L., Forget, F., Millour, E., Venot, O., et al., 2021. Relationship between the ozone and water vapor columns on Mars as observed by SPICAM and calculated by a global climate model. *J. Geophys. Res.* 126 (4), e2021JE006838. <https://doi.org/10.1029/2021JE006838>.
- López-Valverde, M.A., Gerard, J.-C., González-Galindo, F., Vandaele, A.C., Thomas, I., Korablev, O., Ignatiev, N., Fedorova, A., Montmessin, F., Määttänen, A., Guilbon, S., Lefevre, F., Patel, M.R., Jiménez-Monferrer, S., García-Comas, M., Cardesin, A., Wilson, C.F., Clancy, R.T., Kleinböhl, A., McCleese, D.J., Kass, D.M., Schneider, N.M., Chaffin, M.S., López-Moreno, J.J., Rodríguez, J., 2018. Investigations of the Mars upper atmosphere with ExoMars Trace Gas Orbiter. *Space Sci. Rev.* 214 (29). <https://doi.org/10.1007/s1214-017-0463-4>.
- Luginin, M., Fedorova, A., Ignatiev, N., Trokhimovskiy, A., Shakun, A., Grigoriev, A., Patrakee, A., Montmessin, F., Korablev, O., 2020. Properties of water ice and dust particles in the atmosphere of Mars during the 2018 Global Dust Storm as inferred from the Atmospheric Chemistry Suite. *J. Geophys. Res.* 125 (11), e2020JE006419. <https://doi.org/10.1029/2020JE006419>.
- Maltagliati, L., Montmessin, F., Fedorova, A., Korablev, O., Forget, F., Bertaux, J.-L., 2011. Evidence of water vapor in excess of saturation in the atmosphere of Mars. *science* 333 (6051), 1868–1871. <https://doi.org/10.1126/science.1207957>.
- Maltagliati, L., Montmessin, F., Korablev, O., Fedorova, A., Forget, F., Määttänen, A., Lefevre, F., Bertaux, J.-L., 2013. Annual survey of water vapor vertical distribution and water-aerosol coupling in the Martian atmosphere observed by SPICAM/MEx solar occultations. *Icarus* 223 (2), 942–962. <https://doi.org/10.1016/j.icarus.2012.12.012>.
- McCleese, D.J., Heavens, N.G., Schofield, J.T., Abdou, W.A., Bandfield, J.L., Calcutt, S.B., Irwin, P.G.J., Kass, D.M., Kleinböhl, A., Leovy, C.B., Lewis, S.R., Paige, D.A., Read, P.L., Richardson, M.I., Shirley, J.H., Taylor, F.W., Teanby, N., Zurek, R.W., 2010. The structure and dynamics of the martian lower and middle atmosphere as observed by the Mars Climate Sounder: 1. Seasonal variations in zonal mean temperature, dust and water ice aerosols. *J. Geophys. Res.* 115, e12016. <https://doi.org/10.1029/2010JE003677>.
- McCleese, D.J., Schofield, J.T., Taylor, F.W., Calcutt, S.B., Foote, M.C., Kass, D.M., Leovy, C.B., Paige, D.A., Read, P.L., Zurek, R.W., 2007. Mars Climate Sounder: an investigation of thermal and water vapor structure, dust and condensate distributions in the atmosphere, and energy balance of the polar regions. *J. Geophys. Res.* 112, E05S06. <https://doi.org/10.1029/2006JE002790>.
- Murchie, S., Arvidson, R., Bedini, P., Beisser, K., Bibring, J.-P., Bishop, J., Boldt, J., Cavender, P., Choo, T., Clancy, R., et al., 2007. Compact Reconnaissance Imaging Spectrometer for Mars (CRISM) on Mars Reconnaissance Orbiter (MRO). *J. Geophys. Res.* 112 (E5), e05S03. <https://doi.org/10.1029/2006JE002682>.
- Murchie, S.L., Seelos, F.P., Hash, C.D., Humm, D.C., Malaret, E., McGovern, J.A., Choo, T.H., Seelos, K.D., Buczkowski, D.L., Morgan, M.F., et al., 2009. Compact Reconnaissance Imaging Spectrometer for Mars Investigation and data set from the Mars Reconnaissance Orbiter's primary science phase. *J. Geophys. Res.* 114 (E2). <https://doi.org/10.1029/2009JE003344>.
- Murphy, D.M., Koop, T., 2005. Review of the vapour pressures of ice and supercooled water for atmospheric applications. *Q. J. R. Meteorol. Soc.* 131, 1539–1565. <https://doi.org/10.1256/qj.04.94>.
- Neary, L., Daerden, F., Aoki, S., Whiteway, J., Clancy, R.T., Smith, M., Viscardy, S., Erwin, J.T., Thomas, I.R., Villanueva, G., Liuzzi, G., Crismani, M., Wolff, M., Lewis, S.R., Holmes, J.A., Patel, M.R., Giuranna, M., Depiesse, C., Piccialli, A., Robert, S., Trompet, L., Willame, Y., Ristic, B., Vandaele, A.C., 2020. Explanation for the increase in high-altitude water on Mars observed by NOMAD during the 2018

- Global Dust Storm. *Geophys. Res. Lett.* 47, e2019GL084354. <https://doi.org/10.1029/2019GL084354>.
- Neefs, E., Vandaele, A.C., Drummond, R., Thomas, I.R., Berkenbosch, S., Clairquin, R., Delanoye, S., Ristic, B., Maes, J., Bonnewijn, S., et al., 2015. NOMAD spectrometer on the ExoMars Trace Gas Orbiter mission: part 1—design, manufacturing and testing of the infrared channels. *Appl. Opt.* 54 (28), 8494–8520. <https://doi.org/10.1364/AO.54.008494>.
- Patel, M.R., Antoine, P., Mason, J., Leese, M., Hathi, B., Stevens, A.H., Dawson, D., Gow, J., Ringrose, T., Holmes, J., et al., 2017. NOMAD spectrometer on the ExoMars Trace Gas Orbiter mission: part 2—design, manufacturing, and testing of the ultraviolet and visible channel. *Appl. Opt.* 56 (10), 2771–2782. <https://doi.org/10.1364/AO.56.002771>.
- Rapp, M., Thomas, G.E., 2006. Modeling the microphysics of mesospheric ice particles: Assessment of current capabilities and basic sensitivities. *J. Atmos. Sol. Terr. Phys.* 68 (7), 715–744. <https://doi.org/10.1016/j.jastp.2005.10.015>.
- Shirley, J.H., McConnochie, T.H., Kass, D.M., Kleinböhl, A., Schofield, J.T., Heavens, N.G., McCleese, D.J., Benson, J., Hinson, D.P., Bandfield, J.L., 2015. Temperatures and aerosol opacities of the Mars atmosphere at aphelion: validation and inter-comparison of limb sounding profiles from MRO/MCS and MGS/TES. *Icarus* 251, 26–49. <https://doi.org/10.1016/j.icarus.2014.05.011>.
- Smith, M.D., Wolff, M.J., Clancy, R.T., Kleinböhl, A., Murchie, S.L., 2013. Vertical distribution of dust and water ice aerosols from CRISM limb-geometry observations. *J. Geophys. Res.* 118, 321–334. <https://doi.org/10.1002/jgre.20047>.
- Trompet, L., Mahieux, A., Ristic, B., Robert, S., Wilquet, V., Thomas, I.R., Vandaele, A.C., Bertaux, J.-L., Nov, 2016. Improved algorithm for the transmittance estimation of spectra obtained with SOIR/Venus Express. *Appl. Opt.* 55 (32), 9275–9281. <https://doi.org/10.1364/AO.55.009275>.
- Vandaele, A.C., Korablev, O., Daerden, F., Aoki, S., Thomas, I.R., Altieri, F., López-Valverde, M., Villanueva, G., Liuzzi, G., Smith, M.D., et al., 2019. Martian dust storm impact on atmospheric H₂O and D/H observed by ExoMars Trace Gas Orbiter. *Nature* 568 (7753), 521–525. <https://doi.org/10.1038/s41586-019-1097-3>.
- Vandaele, A.C., Lopez-Moreno, J.-J., Patel, M.R., Bellucci, G., Daerden, F., Ristic, B., Robert, S., Thomas, I., Wilquet, V., Allen, M., et al., 2018. NOMAD, an integrated suite of three spectrometers for the ExoMars Trace Gas mission: Technical description, science objectives and expected performance. *Space Sci. Rev.* 214 (5), 80. <https://doi.org/10.1007/s11214-018-0517-2>.
- Whiteway, J.A., Konguem, L., Dickinson, C., Cook, C., Illnicki, M., Seabrook, J., Popovici, V., Duck, T.J., Davy, R., Taylor, P.A., Pathak, J., Fisher, D., Carswell, A.I., Daly, M., Hipkin, V., Zent, A.P., Hecht, M.H., Wood, S.E., Tamppari, L.K., Renno, N., Moores, J.E., Lemmon, M.T., Daerden, F., Smith, P.H., 2009. Mars water-ice clouds and precipitation. *Science* 325, 68–70. <https://doi.org/10.1126/science.1172344>.
- Zurek, R.W., Smrekar, S.E., 2007. An overview of the Mars Reconnaissance Orbiter (MRO) science mission. *J. Geophys. Res.* 112, e05S01. <https://doi.org/10.1029/2006JE002701>.